Journal of Machine Engineering, 2024, Vol. 24
ISSN 1895-7595 (Print) ISSN 2391-8071 (Online)

Received*: 19 June 2024* / Accepted: *13 November 2024* / Published online: *04 October 2024*

Ti6Al4V, SPH, machining, textured tools

Hagen KLIPPEL[1*], Fabian KNEUBÜHLER[1]
Livia HAUDENSCHILD[1], Nanyuan ZHANG[1]
Michal KUFFA[1], Konrad WEGENER[1]

AN ATTEMPT FOR NUMERICAL OPTIMISATION OF A MICRO-GROOVE GEOMETRY AT THE RAKE FACE WHEN TURNING Ti6AL4V ALLOY WITH INDEXABLE INSERTS

Machining of Ti6Al4V is considered difficult because the material removal rates are relatively small if the tool wear shall be low. In recent years the reduction of process forces as well as tool wear have been investigated by introducing textures (pockets) into the tool surface. To advance the understanding how those textured tools function and to reduce the experimental effort, a smoothed particle hydrodynamics (SPH) model of the orthogonal cutting process with a parametrised tool containing a single pocket on the rake face with variable position and depth is presented. This simulation model is used to enhance the understanding of a rake face groove in order to design optimum cutting tools for given process parameters. Using an optimisation algorithm, an optimum groove geometry is determined numerically and is then experimentally validated, followed by a discussion, why process force reductions are lower than predicted.

1. INTRODUCTION

Machining of Titanium alloys such as Ti6Al4V due to their high strength and low thermal conductivity, which results in increased tool wear. This issue can be accommodated by reducing cutting speeds, but this leads to higher processing times and limits productivity [1]. Recent research [2, 3] suggests modifications of cutting edges using textures, which require special techniques to enable material removal at the micrometer scale with high accuracy on the cutting tool surface. Ultra short pulsed laser ablation techniques meet these requirements effectively, offering minimal thermal impact on the tool. Textured tools have to potential to reduce process forces and decrease coolant consumption or even enable dry cutting while maintaining or improving tool life. Rake face modifications can lower the generated heat by reducing friction at the tool-chip interface. In [4] process force reductions of up to 31% are shown for textured tools using grooves, while [5] reports cutting force reductions of up to 38% using dimples on the rake face. The investigation in [6] reports feed

[1] IWF, ETH Zürich, Switzerland
[*] E-mail: hklippel@ethz.ch
https://doi.org/10.36897/jme/193264

force reductions of up to 50% using a line texture on the rake face and it is observed that the texture can store wear debris, thus reducing wear and friction. Similar results are reported in [7] in dry cutting. Textures can also be used to direct coolant fluids closer to the cutting edge and improve its spread. For example, [8] reports a 20% reduction in cutting force compared to an unmodified tool with flood lubrication. Using a bionic microtexture (BMT), inspired from a Nepenthes' peristome from nature, and microgroove textures (MGT), cutting force reductions of up to 80% are found by [9]. When the texture is applied on the flank face, it was observed in [10] that cutting and feed forces reduce by 8% and 12%, respectively.

Designing such textures is however at the current state an iterative procedure, which requires many experiments with a trial and error approach. This investigation aims to enhance the understanding and optimise a rake face groove, which can be seen as a restricted contact tool (RCT) according to [11]. The optimisation is carried out using numerical methods for a constant set of process conditions. For this purpose a reference dry orthogonal cutting test is performed and used in a first step to identify the constitutive model constants of the used material batch of Ti6Al4V with inverse methods in a smoothed particle hydrodynamics (SPH) model of the orthogonal cutting test. In the following step, these material parameters are used in a second SPH simulation model with a parametrised rake face groove, and the geometry, which minimises the process forces, is then determined with an optimisation algorithm. This rake face groove is subsequently applied to the original cutting insert by laser ablation and the predicted process force reductions are then validated in a second cutting experiment.

2. MATERIALS AND METHODS

2.1. EXPERIMENTAL SETUP

Dry orthogonal cutting experiments are carried out using a planning setup on a 5 axis CNC milling machine Fehlmann Versa 825. Forces are measured with a piezoelectric dynamometer, Kistler 9257A, which holds the tool holder and is mounted stationary on the machine table, while the workpiece holder moves in z-direction [12]. The setup is illustrated in Fig. 1.

A reference cutting test is performed on a strip of Ti6Al4V material with a length of 200 mm and a width of 2.43mm. An unmodified tool Sandvik CCMW 09 T3 04 H13A (ISO) is used with a clearance angle of $\alpha_0 = 7°$ and rake angle of $\gamma_0 = 0°$. Since the cutting edge radius is unspecified by the manufacturer, the entire cutting edge of the insert is scanned before the cutting experiment with a Sensofar S NEOX microscope using the focus variation principle. The cutting edge radii along the edge is evaluated with the method in [13]. Similar to [14], the averaged cutting edge radius along the width of cut is computed after the test and results in $r_\beta = 28.6\ \mu m$ with a standard deviation of $\sigma_{r_\beta} = 1.6\ \mu m$. An image of the cutting edge and the radius variation along the whole edge is shown in Fig. 2. The cutting test is conducted with a cutting speed of $v_c = 30\ m/min$ and a feed (uncut chip thickness) of f=100 μm, while the process forces are measured.

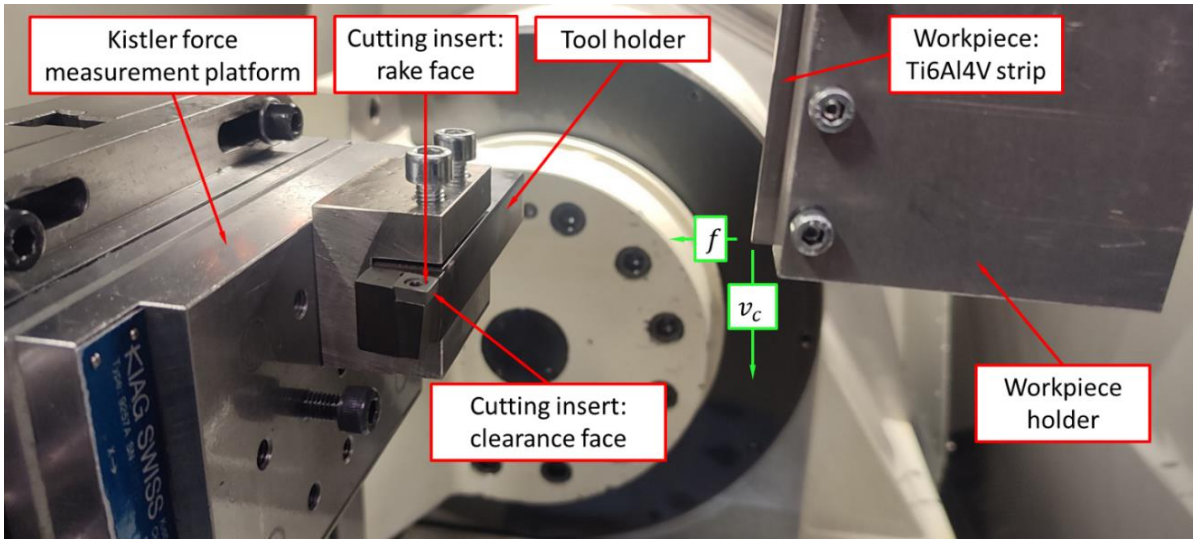

Fig. 1. Orthogonal cutting setup used in this work

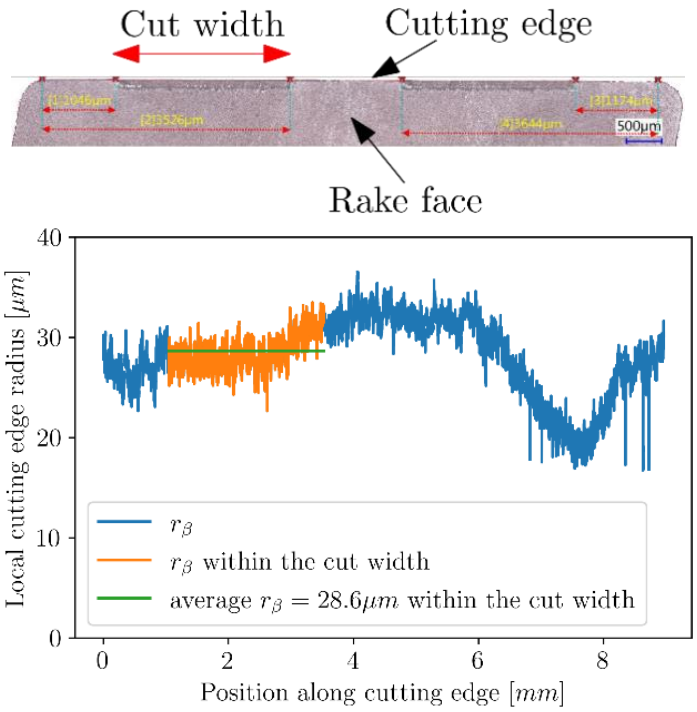

Fig. 2. Cutting edge of the reference experiment after the cut test (top) and cutting edge radii along the cutting edge (bottom) with the average cutting edge radius along the cut width marked in green

The averaged cutting and feed force are $F_c^{exp} = 226.4\,\mathrm{N/mm}$ and $F_f^{exp} = 146.2\,\mathrm{N/mm}$, respectively. Using the method described in [15] an averaged chip thickness is determined as $h_{avg} = 102$ µm with a standard deviation of $\sigma_{h_{avg}} = 7$ µm from an etched chip section. A picture of the chip section of this experiment is provided in Fig. 3 together with the local chip thicknesses along the chip length. The chip form is wavy, but no pronounced segmentation behaviour is visible.

Table 1. Tool geometry, process conditions, measured forces and average chip thickness in the orthogonal cutting test

Tool geometry			Process conditions and measured forces				Average chip thickness
α_0	γ_0	r_β	v_c	f	F_c^{exp}	F_f^{exp}	h_{avg}
[°]	[°]	$[\mu m]$	$[m/min]$	$[\mu m]$	$[N/mm]$	$[N/mm]$	$[\mu m]$
7	0	28.6	30	100	226.4	146.2	102.3

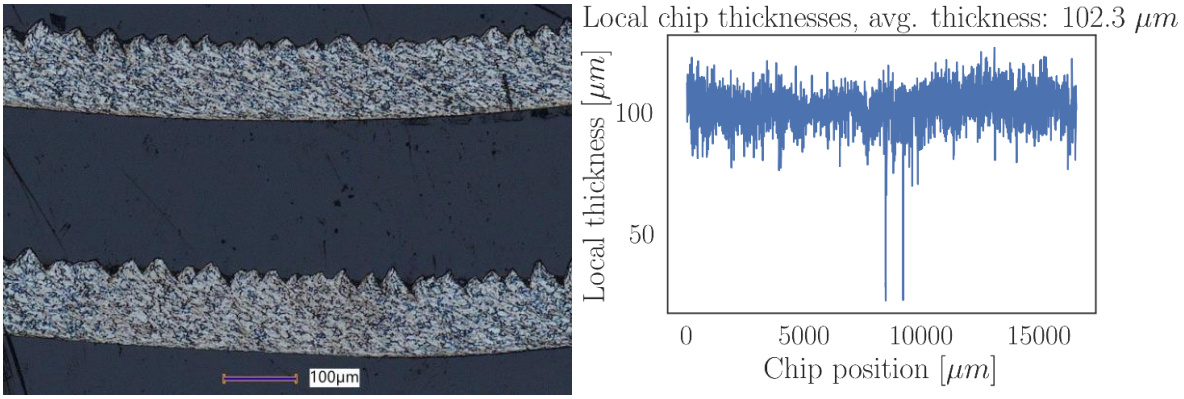

Fig. 3. Close-up of the embedded chip from the reference experiment (left) which is used to compute the local chip thickness distribution along the chip (right)

2.2. SMOOTHED PARTICLE HYDRODYNAMICS

2.2.1. THEORETICAL BACKGROUND

The SPH was introduced 1977 in astrophysics Gingold and Monaghan [16] for the calculation of a smoothed density from point clouds. A simple derivation of the method is based on the partition of unity [17], where a field value at a spatial location x can be determined as:

$$f(x) = \int_{\mathbb{R}^d} \delta(x - x') f(x') d\Omega_{x'} \quad \forall x \epsilon \mathbb{R}^d \tag{1}$$

The Dirac-delta function $\delta(x)$ in equation (1) has two important properties:

$$\int_{-\infty}^{+\infty} \delta(x) dx = 1 \tag{2}$$

$$\int_{-\infty}^{+\infty} \delta(\zeta - x) f(\zeta) d\zeta = f(x) \tag{3}$$

Replacing the Dirac-delta function $\delta(x)$ with a smoothing function, the so-called Kernel $W(x - x', h)$; e.g., the Gauß-function, with h being a smoothing length, the behavior of the Dirac-delta can be reproduced for the limit:

$$\lim_{h \to 0} W(x - x', h) = \delta(x - x') \tag{4}$$

Inserting (4) into equation (3) gives an approximation of the function value $f(x)$ at x:

$$< f(x) >= \int_{-\infty}^{+\infty} W(x - x', h) f(x') dx' \tag{5}$$

The integration is approximated by a Riemann-sum within a discrete neighbourhood:

$$< f_i >= \sum_j f_j \, W\big(x_{ij}, h\big) \Delta V_j \tag{6}$$

with the point index i at which the function value is to be approximated by its neighbour points j, x_{ij} is the spatial distance between point i and j and ΔV_j being an integration weight of point j. Computation of the function's derivative leads to

$$< \nabla f_i >= \sum_j f_j \, \nabla W\big(x_{ij}, h\big) \Delta V_j \tag{7}$$

where only the derivative of the Kernel $W\big(x_{ij}, h\big)$ is required. In this way, derivatives of values given at point cloud locations can be computed without the requirement of a functional description or a mesh-based relation between these points (particles). With this meshfree approximation, derivatives in the continuum mechanics equation can be computed by sums of discrete values in the neighbourhood of the particles. Meshfree techniques were adopted in the early 1990s to structural simulations [18] and for numerical cutting simulations first in [19]. At the institute of machine tools and manufacturing (IWF) of ETH Zürich, the software iMFREE was developed in the past years for SPH-based machining simulations [20]. The software is capable of performing CPU as well as GPU-enhanced computations of metal cutting simulations with high efficiency. It establishes the state-of-the-art in SPH simulations as it facilitates the most recent correctors and stabilization measures [21]. A recent overview of the capabilities of the software package is provided in [22]. Lately, it was extended with a SPH-FEM coupling for efficient tool heat transfer modelling [23] and an extension for the modelling of tool wear during the simulation using an FEM tool model [24] or to investigate the influence of friction modelling with regards to the friction coefficient and its effect to the process forces [25].

In this investigation, the software is used to simulate orthogonal cuts with a flow stress model according to Johnson and Cook (JC) [26]. The model is commonly used to describe metal plasticity within machining simulations and is given as:

$$\sigma_Y = \left(A + B \cdot \varepsilon_{pl}^n\right) \cdot \left(1 + C \cdot ln \frac{\dot{\varepsilon}_{pl}}{\dot{\varepsilon}_{pl}^0}\right) \cdot \left(1 - \frac{T - T_{ref}}{T_f - T_{ref}}\right)^m \tag{8}$$

Herein A, B, C, m and n are material parameters, ε_{pl} the current plastic strain, $\dot{\varepsilon}_{pl}$ the current plastic strain rate and T the current temperature. T_f is the melting temperature, T_{ref} is the reference temperature and $\dot{\varepsilon}_{pl}^0$ the reference plastic strain rate. The first two factors describe hardening due to plastic strain and plastic strain rate, respectively. The third factor controls thermal softening upon increasing temperature. In this investigation, JC material parameters for Ti6Al4V are first identified using inverse parameter identifications with the methods described in [27] and then applied to the optimization of the groove on the rake face.

2.2.2. THEORETICAL BACKGROUND

A parametrised numerical model in 2D is created for simulation the orthogonal cutting of Ti6Al4V using the plane strain assumption. The geometry of the numerical model is depicted in Fig. 4. The cutter is modeled as a rigid body, with an analytical description of the cutter geometry, comprising the clearance angle α_0, rake angle γ_0, and the cutting edge radius r_β. The workpiece is discretized with particles, where the model height w and the model length l are related to the feed *f* (uncut chip thickness) by *w*=3*f*=300 µm and l=10*f*=1000 µm, respectively. Along height and length direction 50×151 particles are used, giving a total number of particles of 7750. The workpiece is restrained on the right side, the bottom side and the lower half of the left side.

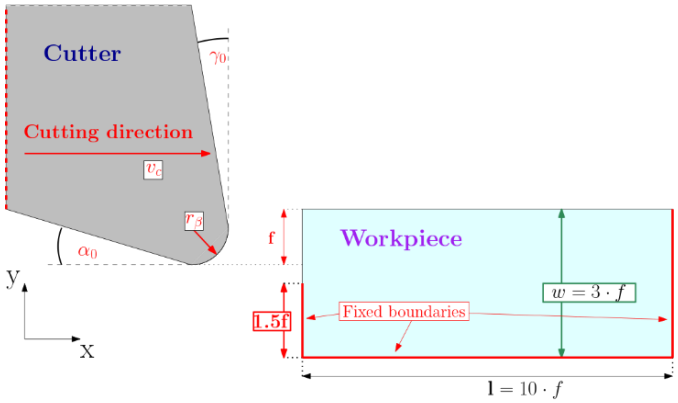

Fig. 4. Basic geometry of the numerical model of the orthogonal cut, from [28]

Plastic dissipation into heat is considered with a Taylor-Quinney coefficient of $\eta_{TQ} = 0.9$ and heat conduction is considered in the workpiece and chip only. Friction between tool and workpiece is modelled with a Coulomb model and a friction coefficient of $\mu_{fr} = 0.35$ according to [29] is applied without consideration of frictional heating. The physical material properties, which are used in the simulations, are given in Table 2.

Table 2. Physical material properties used in the simulations

	Physical properties					JC reference data			Others	
Symbol	E	ν	ϱ	λ	c_p	T_{ref}	T_{melt}	$\dot{\varepsilon}_{pl}^0$	η_{TQ}	μ_{fr}
Unit	[GPa]	[–]	$\left[\frac{\mathrm{kg}}{\mathrm{m}^3}\right]$	$\left[\frac{\mathrm{W}}{\mathrm{mK}}\right]$	$\left[\frac{\mathrm{W}}{\mathrm{mK}}\right]$	[K]	[K]	$[\mathrm{s}^{-1}]$	[–]	[–]
Value	129.4	0.3521	4430	6.8	526	300	1836	1	0.90	0.35
Source	Measured for this batch of Ti6Al4V at EMATronics		[30]	[30]	[30]				[31]	[29]

2.2.3. TOOL MODEL WITH RAKE FACE GROOVE

For the numerical simulation of a tool with a rake face groove, the tool from chapter 2.2.2. is modified with a parametrised pocket, so called “Täschli” [12]. It is modelled as rigid

with an analytical representation of its contour. In addition to rake angle, clearance angle and cutting edge radius, it uses a simplified description of a rake face pocket with only three parameters to make an efficient optimisation feasible. With these three parameters it considers a pocket with variable distance to the cutting edge w_{r_β}, width of the pocket w_T and radius r_T with which the depth of the pocket is defined, see Fig. 5. The minimum radius r_T is bound to $r_T \geq \frac{w_T}{2}$. The workpiece model itself remains unchanged.

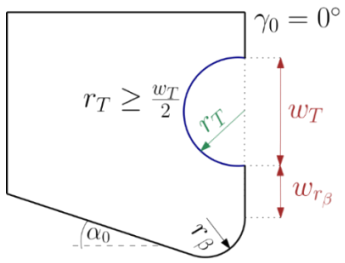

Fig. 5. Parametrised tool with rake face groove "Täschli" and its main dimensions

3. INVERSE IDENTIFICATION OF MATERIAL PARAMETERS

In order to predict the process forces most accurately, an inverse parameter identification is used to derive the JC material parameters of this batch of Ti6Al4V. The structogram of the inverse parameter identification is given in Fig. 6.

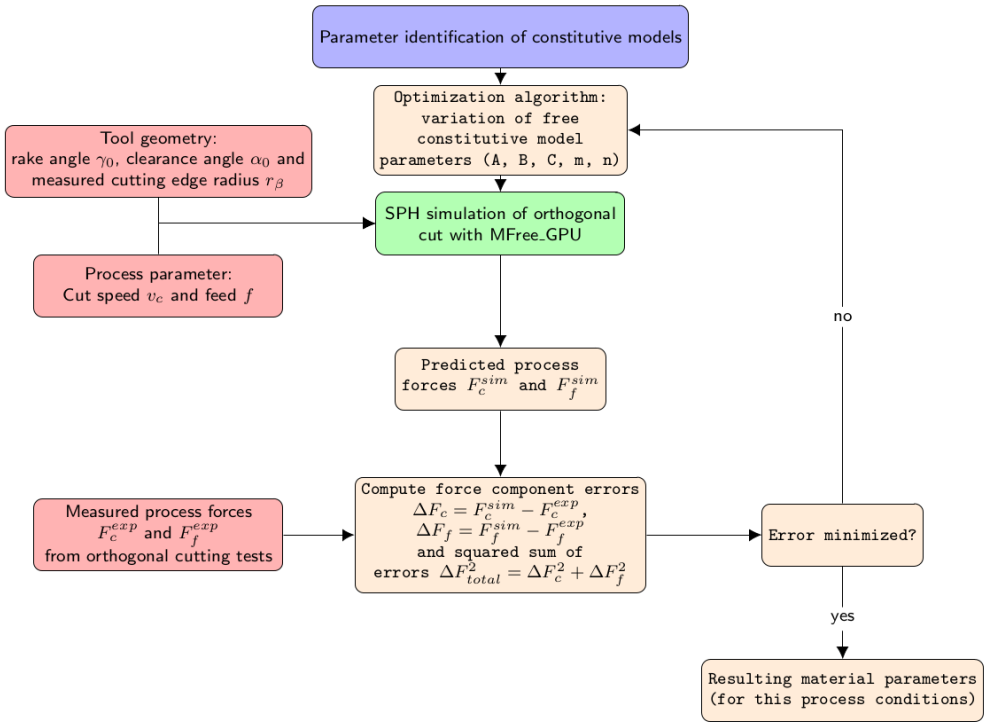

Fig. 6. Structogram of the inverse identification of the JC parameters, adapted from [27]

Input to the inverse identification are the tool geometry $(\alpha_0, \gamma_0, r_\beta)$, the process parameters (v_c, f) and the measured process forces (F_c^{exp}, F_f^{exp}) from the reference experiment in Table 1. The objective function is constructed from the summed squares of the differences in the process force components between simulation and experiment:

$$\begin{aligned} \Delta F_c &= F_c^{sim} - F_c^{exp} \\ \Delta F_f &= F_f^{sim} - F_f^{exp} \\ \Delta F_{\text{total}}^2 &= \Delta F_c^2 + \Delta F_f^2 \end{aligned} \tag{9}$$

The differential evolution algorithm [32] is used with parameter limits for the JC material model according to Table 3, which are derived from ranges provided in [33].

The optimisation is run over 1400 iterations. The best identified parameter set is detailed in Table 4, along with the simulated process force components and its errors compared to the experimental results. The errors for the cutting and feed force components are $\Delta F_c / F_c^{exp} = -1.5\%$ for the cutting force and $\Delta F_f / F_f^{exp} = -23.8\%$ for the feed force component.

Table 3. Parameter boundaries for the JC constitutive model constants within the inverse parameter identification

JC-parameter	*A*	*B*	*C*	*m*	*n*
Unit	[MPa]	[MPa]	[–]	[–]	[–]
Min. value	500	200	0,01	0,3	0,05
Max. value	1500	1200	0,15	0,9	0,99

Table 4. Inversely identified JC material parameters and simulated process forces

A	B	C	m	n	F_c^{sim}	F_f^{sim}	$\Delta F_c / F_c^{exp}$	$\Delta F_f / F_f^{exp}$
[MPa]	[MPa]	[–]	[–]	[–]	[N/mm]	[N/mm]	[%]	[%]
1199.8	1120.4	0.0857	0.3697	0.0862	223.4	111.4	−1.5	−23.8

In Fig. 7 the sensitivities of the cutting and feed force errors with regards to the 5 JC material parameters are shown for the 1400 iterations of the inverse parameter identification.

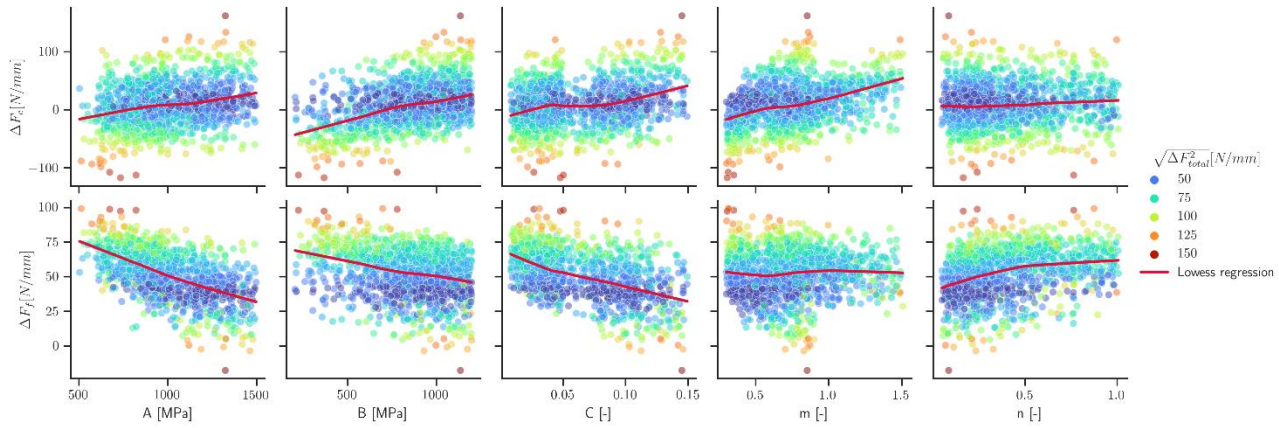

Fig. 7. Sensitivities of the cutting and feed force errors with respect to the JC material parameters from 1400 iterations of the inverse parameter identification together with Lowess regression lines in red. The coloured dots indicate the total force error $\sqrt{\Delta F_{total}^2}$

Lowess regression lines show opposing trends on the force component errors with regards to the material parameters A, B and C, while for parameter m indifferent behaviour to ΔF_f, and for parameter n an indifferent trend for ΔF_c is visible.

In Fig. 8 the contact pressure distribution is shown with the measured chip contact length on the tool together with the local chip thickness measurements. The chip contact length is about 146 µm and chip thicknesses range from 95–100 µm which is slightly lower than in the reference experiment illustrated in Fig. 3.

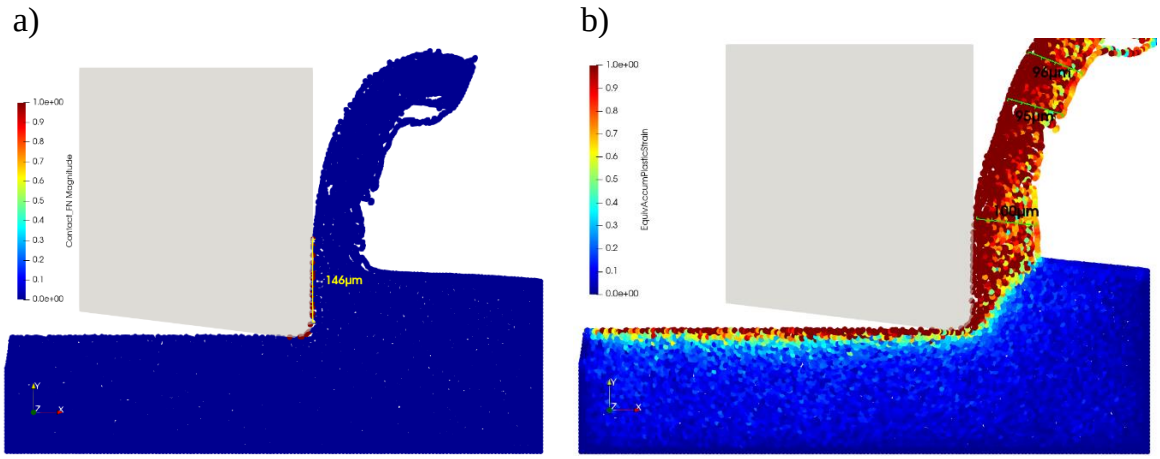

Fig. 8. Determination of the chip contact length from particle contact force results (a) and equivalent plastic strain distribution with chip thickness measurements (b) computed with the optimum JC parameter set from the inverse identification procedure

4. OPTIMISATION OF A RAKE FACE GROOVE GEOMETRY AND POSITION

It is numerically analysed, which pocket geometry promises the highest reductions in process forces. For this purpose, an adapted SPH simulation model is set up using a parametrised rake face pocket, see Fig. 5. The inversely identified JC parameters from Table 4 are used in the simulation. The objective function for the optimisation is constructed from the squared sum of the cutting and feed force: $F_{\text{total}}^2 = (F_c^{sim})^2 + \left(F_f^{sim}\right)^2$ with the goal of minimising F_{total}^2. The differential evolution optimisation algorithm is used for the minimisation of the objective function. The structogram of the optimisation process is shown in Fig. 9.

The three geometrical features of the rake face pocket that are varied in the optimisation are limited to the ranges provided in Table 5. The limits for w_{r_β} are set to ensure that the groove starts within the chip contact length of about 150 µm, enabling an effective reduction of the contact area. The pocket width w_T and radius r_T are limited at the lower bounds in the range of the laser spot diameter ($\approx$ 25 µm), while the upper bounds are chosen to cover the entire chip contact zone.

The optimisation is run with 151 iterations and the pocket geometry promising the highest process force reductions are given in Table 6, and a dimensioned sketch of the pocket is provided with Fig. 10.

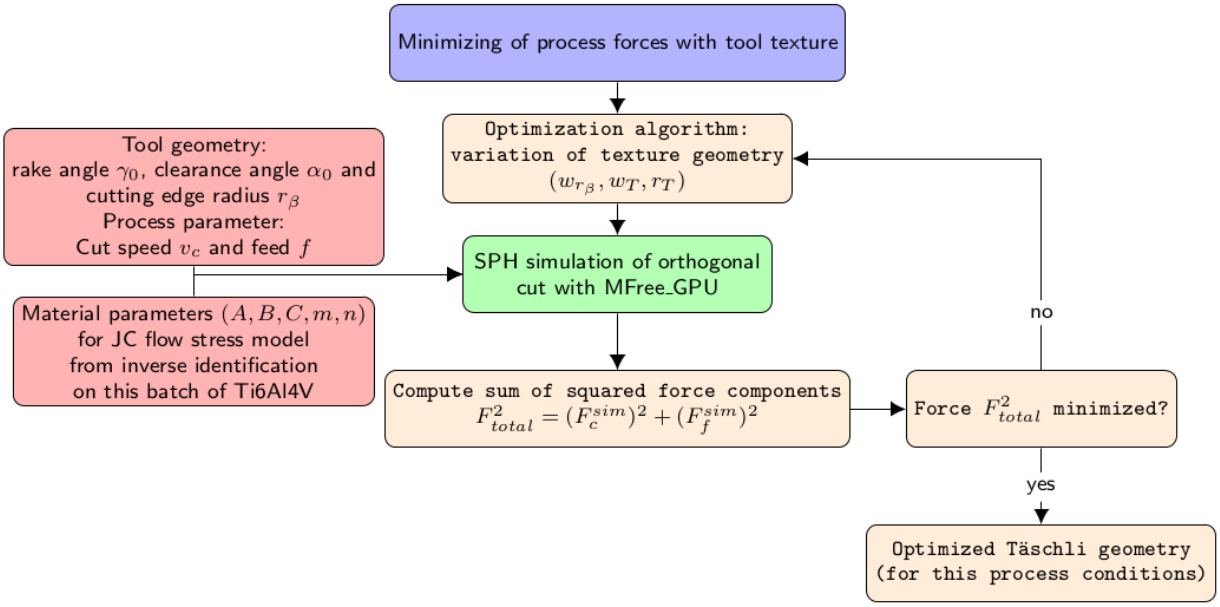

Fig. 9. Structogram of the rake face pocket geometry optimisation

Table 5. Limits for the tool groove geometry optimisation

	w_{r_β}	w_T	r_T
	$[\mu m]$	$[\mu m]$	$[\mu m]$
Minimum	70	40	20
Maximum	150	200	100

Table 6. Tool rake face groove geometry from optimisation using a SPH model and predicted process force reductions

Tool geometry			Tool groove			Process conditions and predicted forces				Process force reduction	
α_0	γ_0	r_β	w_{r_β}	w_T	r_T	v_c	f	F_c	F_f	ΔF_c	ΔF_f
[°]	[°]	$[\mu m]$	$[\mu m]$	$[\mu m]$	$[\mu m]$	$[m/min]$	$[\mu m]$	$[N/mm]$	$[N/mm]$	$[N/mm]$	$[N/mm]$
7	0	28.6	82.4	172.2	86.1	30	100	207.3	83.4	−16.1 (−7%)	−28 (−25%)

The start position of the pocket is found best at a distance of $w_{r_\beta} = 82\ \mu m$ from the end of the cutting edge radius at the rake face with a width of $w_T = 172$ µm and a radius of $r_T =$ 86 µm. In relation to the lowest point of the cutting edge, the start of the pocket is determined with the optimisation at a distance of $r_\beta + w_{r_\beta} = 111$ µm, which is approximately 10% higher than the feed of $f = 100$ µm for which the pocket is optimised.

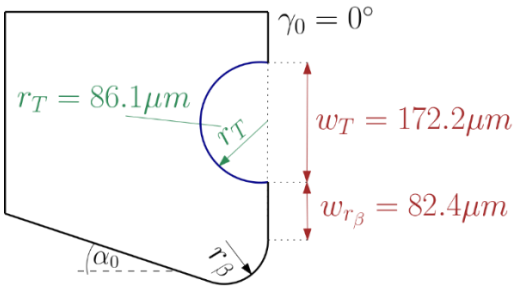

Fig. 10. Dimensioned sketch of the optimised rake face pocket

The predicted process force reductions in comparison to the reference simulation from Table 4 are -7% for the cutting force and -25% for the feed force. The feed force reduction can be attributed to the artificially reduced chip contact length. This leads to decreased friction between tool and chip, and therefore less work is required to cut the material. Consequently, the cutting force reduces as well.

Revisiting all iterations of the pocket optimisation, it can be seen Fig. 11 that the highest force reductions have a minimum at $w_{r_\beta} = 82.4$ µm distance to the cutting edge radius. For the pocket width w_T and the radius r_T, higher values are preferable. In contrast to the inverse identification of material parameters in Fig. 7, adverse effects between cutting and feed force to the pocket position and size do not occur. Both force components tend to decrease with increasing pocket width w_T and radius r_T. The optimal distance of the pocket begins from the cutting edge radius is approximately $w_{r_\beta} = 80$ µm.

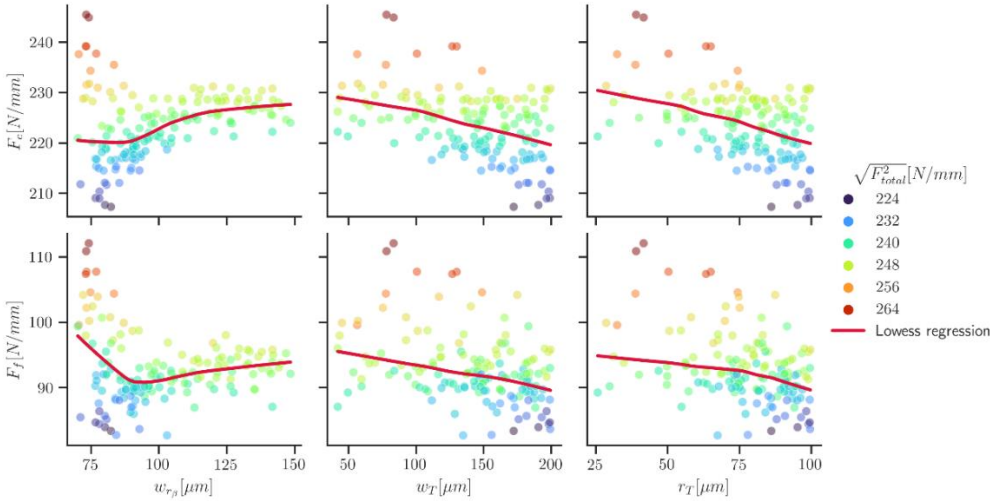

Fig. 11. Sensitivities of the cutting and feed force component to the pocket position and size. The colouring indicates the total force and the red line is a Lowess regression to display the respective trends to the process force component

The chip thickness is predicted to lie within a range from $85 \ldots 91$ µm with the optimised rake face groove, which is a reduction of about 10% compared to the simulation without rake face groove. The predicted chip shape with the plastic strain distribution and thickness measurements is shown in Fig. 12.

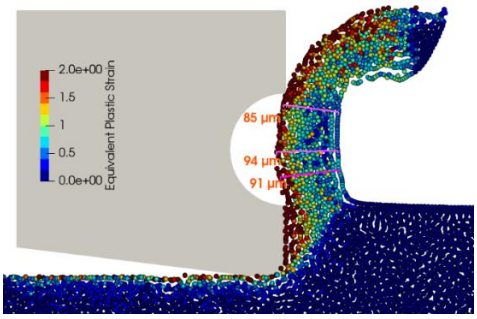

Fig. 12. Equivalent plastic strain distribution and chip thickness measurements computed with the optimised rake face pocket

5. EXPERIMENTAL VALIDATION AND DISCUSSION

The numerically found optimum rake face groove geometry from Table 6 is manufactured using an EWAG Laserline with a pico second laser. The same insert and cutting edge from the reference experiment has been used for the application of the rake face groove to reproduce exactly the same conditions as in the reference test, so that potential changes in cutting behavior can only occur due to the modification itself. The laser-modified geometry is shown in Fig. 13. A slight deviation from the desired distance to the cutting edge becomes evident where the distance from the lowest point of the cutting edge to the pocket begin is $120\mu m$, instead of $r_\beta + w_{r_\beta} = 111$ µm. One potential reason is the variation of the cutting edge radius along the cutting edge between 20 µm to ~35 µm, see Fig. 2, which directly influences the uncertainty of positioning the pocket in the laser machine. Another cause of uncertainty stems from the correct identification of the pocket start in the microscopic measurement of the laser-processed surface, as a running-in behaviour of the laser appears on the borders of the lasered pattern, which makes the correct identification difficult and subjective. For this reasons and considering manufacturing and measurement tolerances of the machine and microscope, the deviation of 9 µm for the pocket start is arguably small, but lower process force reductions are to be expected in the cutting experiment as can be seen from the numerically predicted trends in Fig. 11.

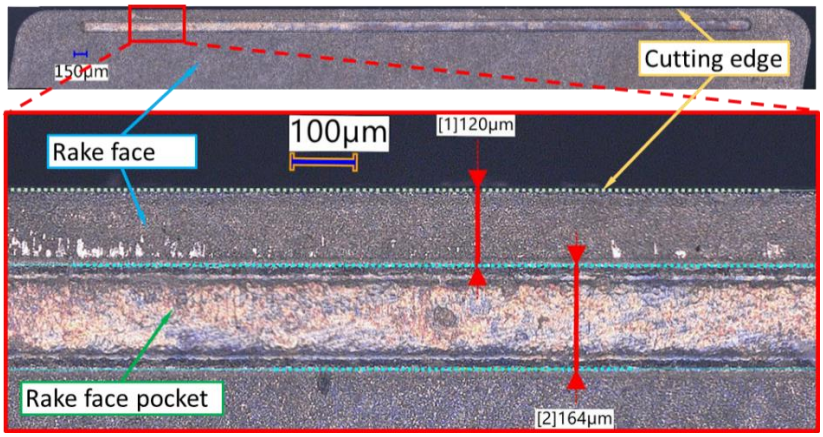

Fig. 13. Laser modified cutting edge: view on the rake face with the cutting edge on top and close-up with distance and width measurement of the pocket

The cutting experiment is repeated with the same process conditions as in the reference experiment, using the modified insert and the process forces are recorded. In total 10 planning strokes are performed. The experimentally measured process forces are shown in Table 7 and it can be seen, that with increasing number of planing strokes the process forces increase. Initially, a reduction of -6.9% and -5.5% is achieved in the cutting and feed force component, respectively. The cutting force reduction is in line with the prediction of the numerical pocket optimization, but the feed force reduction is only around $1/3$ of the prediction. However, reductions reduce with every stroke and in the 10^{th} stroke the reduction is only -1.3% and -2.7% for cutting and feed force component, respectively.

Table 7. Tool geometry, process conditions and measured process forces in the orthogonal cutting experiments with unmodified (reference) and modified tool

Tool geometry			Process conditions		Process forces reference experiment		Process forces with modified insert		Process force reductions		
α_0	γ_0	r_β	v_c	f	F_c	F_f	F_c	F_f	ΔF_c	ΔF_f	Planing stroke
[°]	[°]	[μm]	[m/min]	[μm]	[N/mm]	[N/mm]	[N/mm]	[N/mm]	[N/mm]	[N/mm]	[−]
7	0	28.6	30	100	226.4	146.2	210.8	138.2	−15.6 (−6.9%)	−8 (−5.5%)	1st stroke
							217.6	141.1	−8.8 (−3.9%)	−5.1 (−3.5%)	3rd stroke
							223.4	142.3	−3 (−1.3%)	−3.9 (−2.7%)	10th stroke

The chip generated with the rake face groove optimised tool after the 1st stroke is shown in Fig. 14. In comparison to the chips from the reference experiment in Fig. 3, the average chip thickness reduces by around 5% from $h_{avg} = 102$ µm to $h_{avg} = 97$ µm ($\sigma_{h_{avg}} = 10$ µm) with the rake face grooved tool. This reduction is less than the numerically predicted 10%, possibly because the force reductions are lower than numerically predicted. The chip form itself remained wavy without pronounced signs of chip segmentation. In the later strokes, the chip thicknesses varies between $h_{avg} = 96 \ldots 102$ µm, where the measured force reductions are even lower.

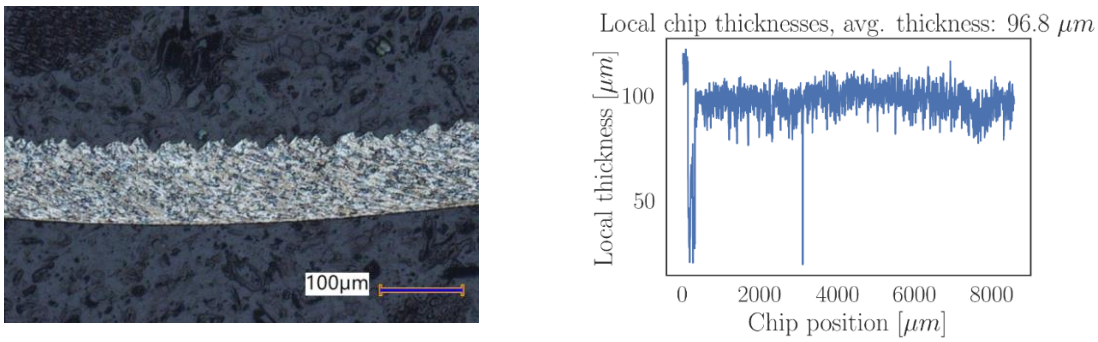

Fig. 14. Embedded chip from the experiment (1st stroke) with rake face groove after the (left) and its local chip thickness distribution along the chip length (right)

After the cutting experiments, debris and adhesion traces are found inside the pocket of the insert, while at the end of the pocket contact traces are seen, see Fig. 15. This suggests that the chip has a second contact with the pocket end.

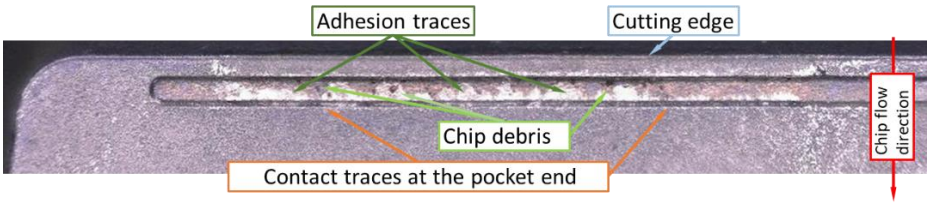

Fig. 15. Top view on the rake face after the cutting experiment. Chip debris and adhesion traces are found inside the rake face pocket as well as contact traces at the end of the pocket

The reasons for the mismatch in the predicted process force reductions is investigated in a refined SPH model (262’404 particles), which is elongated in cutting direction (1.5 mm instead of 1 mm) and with the rake face pocket start at $w_{r_\beta} = 91.4$ µm, as manufactured. In contrast to the former models, heat conduction is modelled in the workpiece, chip and tool, including frictional heating. The simulation results are shown in Fig. 16 together with the process force evolution over time. Debris formation can be seen in the pocket, which means that the end of the pocket acts as a second cutting edge and upon first contact of the chip, the process forces increase and are modulated with the resulting debris thickness.

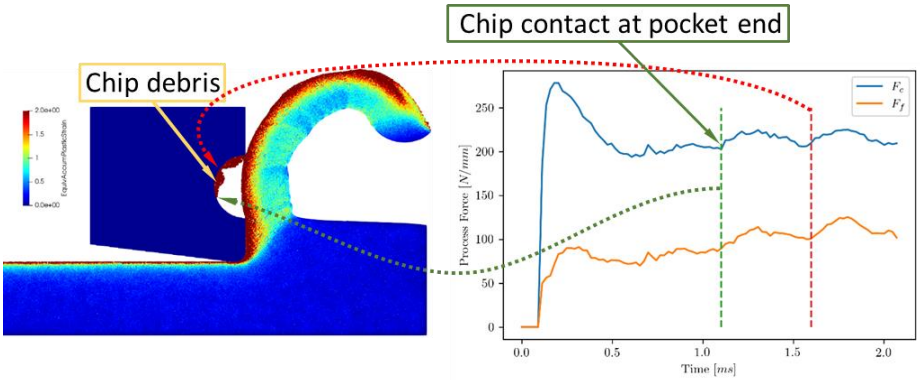

Fig. 16. Recomputation of the manufactured rake face pocket with plastic strain distribution (left) and corresponding process forces (right). When the debris formation starts in the pocket, the simulated process forces increase (green arrow) and fluctuate with the debris thickness (red arrow)

From the findings, it can be concluded that the process force reductions are lower than initially expected, because on the one hand the placement of the pocket begin is about 10% further away from the cutting edge than desired, which reduces the effectiveness of the pocket as indicated in the trends displayed in Fig. 11. On the other hand, the chip has a second contact at the end of the pocket, which leads to a second cutting edge with subsequent process force increases. From a numerical perspective, the simulated cutting length is chosen too short in the pocket optimisation, so that the second tool-chip contact could not be covered fully in the process force evaluation during the optimisation of the pocket. On the other hand, the upper bound of the pocket width w_T in Table 5 is chosen too small in the numerical optimisation and requires an adaptation to enable the chip to leave the pocket without a second tool contact.

6. SUMMARY AND CONCLUSION

In this work, a simulation supported development of a rake face groove in the form of a small pocket is presented. In a first step, orthogonal cutting tests were performed using a planning setup to determine the constitutive material constants for the used batch of Ti6Al4V. This was achieved by using inverse parameter identification within a 2D SPH model of the orthogonal cutting test. With these material parameters, the cutting force was matched with an error of 1.5%, while the feed force error was approximately 24%.

These material constants were then utilised in an optimisation problem, where a parametrised rake face grooved tool was employed in the SPH simulation model. The rake face groove was described using only three parameters, which enabled efficient optimisation. The model aimed to find the optimum geometry of the pocket for a cutting speed of $v_c = 30m/min$ and a feed (uncut chip thickness) of $f = 100$ µm, focusing on reducing process forces by decreasing the chip contact length. The artificially decreased chip contact length led to a decrease in frictional forces, resulting in a lower feed force and, consequently, a reduced cutting force component, as less energy was required for material removal. The optimised pocket geometry from this optimisation was manufactured using laser ablation on the original cutting insert from the reference test. Optical measurements revealed a slightly greater distance from the cutting edge to the beginning of the pocket than desired. This discrepancy was attributed to a less-than-perfect cutting edge, reflected in variations in the cutting edge radii along the cutting edge, and the run-in behaviour of the laser spot during the ablation process, which caused minor deviations at the pocket borders. Considering manufacturing and measurement tolerances of the machine and microscope, these deviations were deemed acceptable.

The laser-modified insert was then tested in another orthogonal cutting experiment under the same process conditions and on the same strip of Ti6Al4V as in the reference cutting test, with 10 planning strokes. Initially, the numerically predicted cutting force reduction of -7% aligned with the measured reduction of -6.9% in the cutting test. However, the feed force reduction was only -5.5% compared to the numerically predicted value of -25%. As the number of planing strokes increased, the process force reductions further decreased to -1.3% for the cutting force and -2.7% for feed force. Analysis of the modified cutting insert after the cutting test revealed debris and adhesion traces inside the pocket, indicating that the chip had made a second contact at the end of the rake face pocket, leading to higher process forces. Revising the numerical model with an increased simulated cutting length yielded similar findings, suggesting that while the SPH simulation model generally reproduces the physics accurately, improvements are needed.

Specifically, enhancements are required in material modelling and inverse parameter identification of constitutive model constants to better match experimentally measured feed forces. Additionally, increasing the upper bound of the pocket width in the numerical rake face pocket optimisation is necessary to prevent a second tool-chip contact and subsequent force increase. Expanding the domain size of the numerical model would also be required, though this would increase computational time.

With these proposed improvements, the approach presented could be developed into an efficient design method for pocket layout, potentially minimising experimental efforts through the use of SPH simulations. It should be noted that an optimal pocket geometry is valid only for the specific set of process parameters (v_c and f); therefore, optimisation must be performed separately for different cutting speeds and feeds. Further investigations should analyse how the introduced notch affects tool life in the brittle tool material, even though no breakouts were observed during validation experiments. This could be explored numerically by incorporating tool wear evolution in the simulation, as presented in [24], and experimentally by testing significantly longer cutting lengths with both unmodified and modified tools.

ACKNOWLEDGEMENTS

The authors hereby would like to thank the SNF for partial funding of this work from the project "GPU-Enhanced Metal Cutting Simulation Using Advanced Meshfree Methods" under the grant #200021_149436 and the Innosuisse for partial funding within the LaserMod-project under grant 53668.1 IP-ENG. Special thanks go to the associated project partners Fritz Studer AG, EWAG Zweigniederlassung, DIXI Polytools SA, Oerlikon Surface Solutions AG, REGO-FIX AG, HEULE Werkzeug AG for their invaluable contributions in time, resources and expertise. Further thanks are directed to EMATronics for the measurement of the Young's modulus and to Matthias Röthlin and Mohammadreza Afrasiabi in their contributions made to the development of iMFREE.

REFERENCES

[1] PETERS M., Ed., 2010, *Titan und Titanlegierungen*, [3., Völlig neu bearb. Aufl.], 3. Nachdr. Weinheim: Wiley-VCH.
[2] Özel T., BIERMANN D., ENOMOTO T., MATIVENGA P., 2021, *Structured and Textured Cutting Tool Surfaces for Machining Applications*, CIRP Annals, 70/2, 495–518, https://doi.org/10.1016/j.cirp.2021.05.006.
[3] MACHADO A.R., et al., 2021, *State of the Art of Tool Texturing in Machining* , Journal of Materials Processing Technology, 293, 117096, http://doi.org/10.1016/j.jmatprotec.2021.117096.
[4] SIJU A.S., GAJRANI K.K., Joshi S.S., 2021, *Dual Textured Carbide Tools for Dry Machining of Titanium Alloys*, International Journal of Refractory Metals and Hard Materials, 94, 105403, https://doi.org/10.1016/j.ijrmhm. 2020.105403.
[5] BIBEYE JAHAZIEL R., KRISHNARAJ V., SUDHAGAR S., GEETHA PRIYADARSHINI B., 2023, *Improving Dry Machining Performance of Surface Modified Cutting Tools Through Combined Effect of Texture and Tin-WS2 Coating*, Journal of Manufacturing Processes, 85, 101–108, https//doi.org/10.1016/j.jmapro.2022.11.033.
[6] ZHENG K., YANG F., PAN M., ZHAO G., BIAN D., 2021, *Effect of Surface Line/Regular Hexagonal Texture on Tribological Performance of Cemented Carbide Tool for Machining Ti-6Al-4V Alloys*, Int. J. Adv. Manuf. Technol., 116/(9–10), 3149–3162, https//doi.org/10.1007/s00170-021-07636-9.
[7] ZHANG N., YANG F., LIU G., 2020, *Cutting Performance of Micro-Textured WC/Co Tools in the Dry Cutting of Ti-6Al-4V Alloy*, Int. J. Adv. Manuf. Technol., 107/9–10, 3967–3979, https//doi.org/10.1007/s00170-020-05161-9.
[8] CAO T., LI Z., ZHANG S., ZHANG W., 2023, *Cutting Performance and Lubrication Mechanism of Microtexture Tool with Continuous Lubrication on Tool-Chip Interface*, Int. J. Adv. Manuf. Technol., 125/3–4, 1815–1826, https//doi.org/10.1007/s00170-023-10821-7.
[9] CHEN J., LIU D., JIN T., QI Y., 2023, *A Novel Bionic Micro-Textured Tool with the Function of Directional Cutting-Fluid Transport for Cutting Titanium Alloy*, Journal of Materials Processing Technology, 311, 117816, https//doi.org/10.1016/j.jmatprotec.2022.117816.
[10] SHARMA R., PRADHAN S., BATHE R.N., 2023, *Comparison, Validation, and Prediction of Machinability Aspects of Textured and Non-Textured Cutting Inserts*, J. Braz. Soc. Mech. Sci. Eng., 45/2, 76, https//doi.org/10.1007/s40430-022-03953-6.
[11] GRZESIK W., 2017, *Advanced Machining Processes of Metallic Materials: Theory, Modelling and Applications, Second Edition*, Amsterdam, Boston: Elsevier.
[12] KNEUBÜHLER F., et al., 2024, *Enhancing Orthogonal Finishing Machining of Ti6Al4V with Laser Modified Tools*, Int. J. Adv. Manuf. Technol.
[13] WYEN C.F., KNAPP W., WEGENER K., 2012, *A New Method for the Characterisation of Rounded Cutting Edges*, Int. J. Adv. Manuf. Technol, 59/9–12, 899–914, https//doi.org/10.1007/s00170-011-3555-4.
[14] KLIPPEL H., SÜSSMAIER S., KUFFA M., WEGENER K., 2022, *Dry Cutting Experiments Database Ti6Al4V and Ck45*, https//doi.org/10.48550/ARXIV.2209.04197.
[15] KLIPPEL H., PFLAUM S., KUFFA M., WEGENER K., 2022, *Automated Evaluation of Continuous and Segmented Chip Geometries Based on Image Processing Methods and a Convolutional Neural Network*, Journal of Machine Engineering, https//doi.org/10.36897/jme/156091.
[16] GINGOLD R.A., MONAGHAN J.J., 1977, *Smoothed Particle Hydrodynamics: Theory and Application to Non-Spherical Stars*, Monthly Notices of the Royal Astronomical Society, 181/3, 375–389, https//doi.org/10.1093/mnras/ 181.3.375.
[17] LI S., LIU W.K., 2007, *Meshfree Particle Methods*, Springer Science & Business Media.

[18] LIBERSKY L.D., PETSCHEK A.G., 1991, *Smooth Particle Hydrodynamics with Strength of Materials*, Lecture Notes in Physics, 395, 248–257, Berlin, Heidelberg: Springer Berlin Heidelberg, https//doi.org/10.1007/3-540-54960-9_58.
[19] HEINSTEIN M., SEGALMAN D., 1997, *Simulation of Orthogonal Cutting with Smooth Particle Hydrodynamics*, SAND–97-1961, 563721, https//doi.org/10.2172/563721.
[20] RÖTHLIN M., 2019, *Meshless Software Tool to Simulate Metal Cutting Operations by Employing Contemporary Numerical Methods*, ETH Zurich, https//doi.org/10.3929/ETHZ-B-000339533.
[21] RÖTHLIN M., KLIPPEL H., WEGENER K., 2018, *Meshless Methods for Large Deformation Elastodynamics*, https//doi.org/10.48550/ARXIV.1807.01117.
[22] KLIPPEL H., ZHANG N., KUFFA M., AFRASIABI M., BAMBACH M., WEGENER K., 2023, *Imfree: A Versatile Software Tool for Modelling Machining Processes with Particle Methods*, Procedia CIRP, 117, 13–19, https//doi.org/ 10.1016/j.procir.2023.03.004.
[23] ZHANG N., et al., 2023, *Hybrid SPH-FEM Solver for Metal Cutting Simulations on the GPU Including Thermal Contact Modeling*, CIRP Journal of Manufacturing Science and Technology, 41, 311–327, https//doi.org/10.1016/j.cirpj.2022.12.012.
[24] ZHANG N., et al., 2023, *Study on the Effect of Wear Models in Tool Wear Simulation Using Hybrid SPH-FEM Method*, Procedia CIRP, 117, 414–419, https//doi.org/10.1016/j.procir.2023.03.070.
[25] ZHANG N., KLIPPEL H., KNEUBÜHLER F., AFRASIABI M., KUFFA M., WEGENER K., 2024, *Investigation of Friction Modeling on Numerical Ti6Al4V Cutting Simulations*, International Journal of Mechanical Sciences, 274, 109231, https//doi.org/10.1016/j.ijmecsci.2024.109231.
[26] JOHNSON, GORDON R., 1983, *A Constitutive Model and Data for Materials Subjected to Large Strains, High Strain Rates, and High Temperatures*, Proc. 7th Inf. Sympo. Ballistics, 541–547.
[27] KLIPPEL H., 2021, *Constitutive Equations for Simulation of Metal Cutting with Meshless Methods on GPU*', ETH Zurich, https//doi.org/10.3929/ETHZ-B-000527668.
[28] KLIPPEL H., et al., 2022, *Cutting Force Prediction of Ti6Al4V Using a Machine Learning Model of SPH Orthogonal Cutting Process Simulations*, Journal of Machine Engineering, 22/1, 111–123, https//doi.org/10.36897/jme/147201.
[29] CARL-FREDERIK W., 2011, *Rounded Cutting Edges and Their Influence in Machining Titanium*, ETH Zurich, https//doi.org/10.3929/ETHZ-A-007134727.
[30] RÜTTIMANN N., 2012, *Simulation of Metal Cutting Processes Using Meshfree Methods*, ETH Zurich, https//doi.org/10.3929/ETHZ-A-010419383.
[31] DUCOBU F., ARRAZOLA P.-J., RIVIERE-LORPHEVRE E., FILIPPI E., 2021, *On the Selection of an Empirical Material Constitutive Model for the Finite Element Modeling of Ti6Al4V Orthogonal Cutting, Including the Segmented Chip Formation*, Int. J. Mater. Form., 14/3, 361–374, https//doi.org/10.1007/s12289-020-01535-2.
[32] STORN R., PRICE K., 1997, *Differential Evolution – A Simple and Efficient Heuristic for Global Optimization Over Continuous Spaces*, Journal of Global Optimization, 11/4, 341–359, https//doi.org/doi: 10.1023/A:1008202821328.
[33] DUCOBU F., RIVIERE-LORPHEVRE E., FILIPPI E., 2017, *On the Importance of the Choice of the Parameters of the Johnson-Cook Constitutive Model and Their Influence on the Results of a Ti6Al4V Orthogonal Cutting Model*, International Journal of Mechanical Sciences, 122, 143–155, 2017.